EES Batteries

ROYAL SOCIETY OF CHEMISTRY

PAPER

View Article Online
View Journal

Cite this: DOI: 10.1039/d6eb00043f

Effect of nanoparticle surface modification on lithium-ion transport in composite polymer electrolytes

Meghan Burns,[a,b] Musawenkosi K. Ncube,[c] Dan McElheny,[b] Michael Counihan,[a] Larry A. Curtiss,[a] Anh T. Ngo,[a,c] Jordi Cabana[a,b,d] and Sanja Tepavcevic*[a]

Solid-state lithium–metal batteries require electrolytes that combine high ionic conductivity with efficient interfacial transport. In this work, we systematically examine how nanoparticle fillers with distinct chemistries and surface functionalizations govern interfacial Li^+ transport in composite polymer electrolytes (CPEs). Inert Al_2O_3 fillers improve CPE performance through mechanical integrity and interfacial contact with lithium; however, surface modification with γ-methacryloxypropyltrimethoxysilane diminishes these benefits, resulting in reduced electrochemical performance relative to neat Al_2O_3. In contrast, modifying lithium containing $Li_{6.25}Al_{0.25}La_3Zr_2O_{12}$ (LLZO) nanoparticles with the same silane agent substantially impacted cell performance: the interfacial resistance decreased, and the lithium-ion transference number increased, yielding a threefold rise in critical current density to the systems containing modified Al_2O_3. LLZO functionalized with (3-aminopropyl)triethoxysilane in an aprotic solvent exhibited poorer electrochemical performance. Solid-state NMR showed reduced lithium content in both silane-modified LLZO samples, with more pronounced depletion under protic modification. Complementary T_1 measurements revealed a larger fraction of fast-relaxing lithium near the nanoparticle surface, consistent with accelerated local Li-ion dynamics. We attribute performance enhancement with LLZO nanofillers to silane-induced lithium vacancies at or near LLZO surfaces that facilitate interfacial Li^+ motion. These results demonstrate that Li-containing fillers are necessary to achieve interfacial transport improvements even when they do not contribute to bulk Li transport, and that performance is governed by changes in local lithium concentration, interfacial chemistry, and ion dynamics. This work establishes a structure–property relationship between silane functionality and ion transport, providing a practical framework for the future interface design toward enabling continuous bulk transport through Li-containing nanofillers in high-performance solid-state electrolytes.

Received 24th February 2026,
Accepted 21st May 2026

DOI: 10.1039/d6eb00043f

rsc.li/EESBatteries

Broader context

The global transition to electrified transportation and a decarbonized grid relies on developing next-generation batteries that can deliver high energy density without the safety risks of flammable liquid electrolytes. Solid-state lithium batteries are the most promising successors, but their commercial viability is stalled by "interfacial bottlenecks" – where high resistance and sluggish ion transport at the electrode–electrolyte interface restrict overall cell performance. Our research overcomes these challenges by engineering the surface chemistry of lithium-containing nanoparticle fillers within composite polymer electrolytes. Surface-functionalized LLZO nanoparticles significantly reduce interfacial resistance and triple the critical current density, promoting more uniform and efficient lithium-ion transport. Advanced structural analysis reveals that performance gains arise from surface-induced lithium vacancies that accelerate local ion dynamics. By establishing clear relationships between nanoparticle chemistry and ion transport, the study provides a practical design framework for safer, higher-performance solid-state batteries. Implementing such principles enables the translation of laboratory advances into scalable energy storage technologies, supporting the global shift toward sustainable electrification.

Introduction

The increasing demand for high-performance energy storage in transportation has accelerated the development of next-generation batteries designed to overcome the limitations of conventional lithium-ion systems.[1–5] Among these, solid-state batteries (SSBs) employing inorganic or polymer-based solid

---

[a] Materials Science Division, Argonne National Laboratory, Lemont, IL 60439, USA. E-mail: sanja@anl.gov
[b] Department of Chemistry, University of Illinois Chicago, Chicago, IL 60607, USA
[c] Department of Chemical Engineering, University of Illinois Chicago, Chicago, IL 60608, USA
[d] Energy Storage Research Alliance, Argonne National Laboratory, Lemont, IL 60439, USA

electrolytes have emerged as a promising alternative to traditional liquid electrolyte-based batteries, which face well-known safety and stability concerns.[6–8] Lithium metal, with its exceptionally high theoretical specific capacity (3860 mAh g^{-1}) and the lowest electrochemical potential (−3.04 V *vs.* SHE), is widely regarded as an ideal anode material for enabling high-energy density batteries.[1–5] However, its practical implementation remains limited by interfacial instability, dendritic lithium growth, and mechanical degradation at the electrolyte–electrode interface.[2,4,5] Continued progress in interface design, solid-electrolyte engineering, and materials optimization is therefore critical to advancing the performance, safety, and durability of lithium metal solid-state batteries.

Among the strategies to optimize solid electrolyte performance, composite polymer electrolytes (CPEs) have attracted significant interest as promising materials for next-generation energy-storage technologies, including lithium-ion batteries, fuel cells, and supercapacitors.[9–11] Plasticizers are widely incorporated into CPEs to enhance their mechanical and electrochemical properties.[12–15] Polyethylene glycol (PEG) is one of the most widely used among them due to its favorable properties including high ionic conductivity, low melting point, and good mechanical stability.[15–17] Organic solvents such as dimethyl carbonate (DMC), propylene carbonate (PC) and ethylene carbonate (EC) are also used as plasticizers and co-solvents in CPEs.[11,12] DMC exhibits low toxicity and good solvating abilities, while PC provides high polarity, excellent solubility, and thermal stability.[11] EC, with its high dielectric constant and strong Li^+-solvation capability, is particularly effective in improving salt dissociation.[18–20] The plasticizer content in CPEs typically ranges from 10 to 50 wt% of the polymer, depending on the desired mechanical and electrochemical performance.[12–20] For example, PEG loadings of approximately 20 wt% have been shown to significantly enhance the ionic conductivity and improve the mechanical robustness of the electrolyte.[12] In general, the plasticizer identity and content depend on factors such as the polymer chemistry, salt concentration, processing conditions, and targeted performance metrics of the electrochemical device.[9–11]

In addition to plasticizers, the incorporation of nanoparticles represents another effective strategy to improve the mechanical and electrochemical performance of CPEs.[21,22] The dimensions of fillers can vary depending on the application and the desired properties of the composite material, typically ranging from the microscale to nanoscale.[21–24] Particle size strongly influences both ionic conductivity and mechanical properties. Larger fillers can improve mechanical strength and stiffness but may reduce ionic conductivity and increase composite viscosity, hindering ion transport.[24–26] Conversely, smaller nanoparticles offer a higher surface area that can enhance ionic conductivity. However, their strong interparticle interactions and high surface energy can lead to agglomeration, making uniform dispersion in the polymer matrix more challenging.[24–28] Beyond transport and mechanical reinforcement, nanofillers can act as physical barriers against dendrite growth and improve adhesion between the polymer and electrode surfaces, thereby enhancing both performance and safety in lithium-ion batteries.[23,24,29–34]

From a chemical perspective, both Li-containing and non-Li-containing nanofillers can be employed to enhance CPE performance.[24] Non-Li-containing, inert nanofillers such as silica, alumina, and carbon nanotubes can create microstructures within the polymer matrix that improve ion transport and mechanical integrity.[24,29,30] Among inert nanofillers, alumina is the most widely used due to its low cost and electrical insulation properties. With a high elastic modulus, it enhances the mechanical stiffness and robustness of CPEs, at the expense of a lower ionic conductivity and higher inherent brittleness, which constrain the maximum practical loading.[35–39] Whereas inert fillers primarily modify mechanical and structural properties, Li-containing nanofillers introduce additional Li^+ ions and fast conduction pathways.[9] Examples of such fillers include $Li_4Ti_5O_{12}$ and $Li_{1.3}Al_{0.3}Ti_{1.7}(PO_4)_3$, which can enhance electrolyte ionic conductivity,[40,41] and $Li_{6.25}Al_{0.25}La_3Zr_2O_{12}$ (LLZO) nanoparticles, notable for their high intrinsic Li^+ conductivity and chemical stability.[9,24] As nanoscale additives, LLZO provides a high surface area-to-volume ratio that increases interfacial contact with the polymer and electrode, facilitating interfacial Li^+ transport.[42,43] By increasing the density of mobile Li^+ charge carriers and suppressing Li^+-anion pairing, these fillers reduce localized ion depletion and concentration gradients, collectively enhancing ionic conductivity, lowering interfacial resistance, mitigating dendrite formation, and promoting more uniform Li^+ flux for improved cycling stability.[9,24,44–47]

Surface functionalization offers a route to further optimize nanofiller–polymer interactions. Modifying oxide surfaces can improve dispersion, wettability, and interfacial adhesion, thereby lowering interfacial resistance and enhancing mechanical robustness.[48–51] Carboxylic acid groups can anchor polymer segments to oxide surfaces, while amino and hydroxyl groups enhance wettability and promote strong interfacial bonding.[49,50] More broadly, tailored oxide surface chemistries adjust adhesion, biocompatibility, photocatalytic properties, and hydrophobicity, underscoring the versatility of functionalization strategies.[48–52] Although many studies report increased Li^+ conductivity in LLZO–polymer mixtures, direct evidence for Li^+ transport through the LLZO phase remains limited.

In our previous work,[45] we demonstrated that although anhydrous silane functionalization of LLZO nanoparticles and nanofibers improved interfacial transport, the addition of LLZO fillers did not enhance bulk Li^+ transport in PEO–LiTFSI composite electrolytes. Solid-state $^7Li/^6Li$ NMR showed that Li^+ is transported preferentially along the LLZO–PEO interface with negligible contribution from bulk LLZO, indicating that the observed effects are interfacial rather than bulk in origin. Detailed studies of LLZO–polymer composites reveal physicochemical limits to Li^+ exchange at the ceramic–polymer interface, arising from polymer-ion dynamics and reacted LLZO surface layers.[42–45] Here, we systematically examine how nanoparticle attributes (active *versus* inert) and surface functionalization chemistry govern interfacial Li^+ transport at the nanoparticle-PEO boundary. Our objective is to map structure–property relationships spanning polymer dynamics, interphase resistance, and ion selectivity to explain, control, and enhance interfacial conduction, with the longer-term aim of enabling continuous bulk transport through LLZO. Given the prominence of interfacial pathways, we further ask whether inert fillers that provide similar interfacial transport could achieve comparable performance, and if so, whether lithium-containing nanoparticles are truly necessary.

To address this question, in this manuscript we investigated PEO-based CPEs containing 20 wt% tetraethylene glycol dimethyl ether (TEGDME) as a plasticizer and 500 nm either inert aluminum oxide (Al_2O_3) or lithium-rich LLZO nanoparticles, with and without silane functionalization. LLZO nanoparticles were functionalized with γ-methacryloxypropyltrimethoxysilane (A-174) or (3-aminopropyl)triethoxysilane (APTES). The methacrylate-functional A-174 was selected to enhance compatibility between the inorganic filler and the PEO matrix by introducing an organic, moderately polar interphase, whereas APTES was chosen to probe the influence of basic amine groups on lithium-ion coordination and interfacial charge. The addition of 20 wt% TEGDME increased room-temperature ionic conductivity while improving mechanical flexibility and processability. Neat Al_2O_3 increased the Li^+ transference number and critical current density, and decreased the interfacial resistance, although bulk ionic conductivity remained unchanged. Surface modification of Al_2O_3 with γ-methacryloxypropyltrimethoxysilane (A-174@Al_2O_3) produced no improvement relative to the unmodified polymer–salt–plasticizer matrix and performed worse than the neat Al_2O_3. In contrast, incorporating LLZO nanoparticles modified with the same silane (A-174@LLZO) enhanced cell performance: bulk ionic conductivity remained unchanged, interfacial resistance decreased substantially, and a threefold increase in the critical current density relative to the PEO–LiTFSI–TEGDME system was observed. Functionalization of LLZO with (3-aminopropyl)triethoxysilane (APTES@LLZO) led to poorer electrochemical performance compared to A-174@LLZO. Solid-state NMR revealed that both silane-modified LLZO samples had reduced lithium content relative to unmodified LLZO, with a more pronounced depletion in the A-174@LLZO sample. Complementary T_1 measurements showed that A-174@LLZO contained a greater fraction of fast-relaxing lithium populations, indicating enhanced local ion dynamics near the nanoparticle surface. These spectroscopic insights explain all the observed electrochemical behavior: changes in the lithium concentration and local coordination, coupled with accelerated ion dynamics at the interface, promoted improved interfacial transport and a higher transference number, consistent with the reduced interfacial resistance and increased critical current density in A-174@LLZO-containing cells. Collectively, our data shows that Li-containing nanoparticles are indeed necessary to reduce interfacial resistance and improve transport, whereas inert fillers alone provide only mechanical reinforcement.

Experimental/methods

Materials

The 400–600 nm cubic phase Al-doped $Li_{6.25}Al_{0.25}La_3Zr_2O_{12}$ (LLZO) nanoparticles were purchased from MSE supplies, batch number 03923C1. The 500 nm high purity alpha aluminum oxide nanoparticles (Al_2O_3) were purchased from MSE supplies, batch number 35623A3. (PEO (M_v = 600 kDa)), lithium bis(trifluoromethanesulfonyl)imide (LiTFSI, 99.95% metal basis), acetonitrile (ACN, 99.8% anhydrous), toluene (99.8%, anhydrous), and tetraethylene glycol dimethyl ether (TEGDME, 99%) were purchased from Sigma-Aldrich. Methanol (MeOH, HPLC grade), acetic acid (AcOH, glacial, certified ACS), and ethanol (EtOH, 99.5%, ACS reagent) were purchased from Fisher Scientific. Millipore water was used as the water source. Both the silanes used, methacryloxypropyl trimethoxysilane (A-174) and (3-aminopropyl)triethoxysilane (APTES) were purchased from Millipore Sigma. The Li foil used for the electrodes was purchased from MTI with a 250 μm thickness. Li foil electrodes were cleaned with a steel brush and a lint-free cloth to remove surface contaminants, then punched to have an area of 0.9 cm^2. Coin cells were assembled in 2032 stainless steel coin cells with one 1.0 mm and one 0.5 mm thick stainless-steel spacer. To create homogeneous pressure in the cell, a piece of rubber (McMaster Carr) covered in copper foil (Cu, 6 μm thick, MSE supplies) was added to the cell stack.

APTES silane modification of LLZO (APTES@LLZO) was carried out by dispersing 1 g of LLZO nanoparticles in 80 mL of toluene in a round-bottom flask inside a glovebox. After adding 3 mL of APTES, the mixture was stirred and refluxed under nitrogen for 24 hours. The now functionalized particles were then centrifuged, washed several times with ethanol, and dried for 72 hours to remove excess APTES. The A-174 silane modification of LLZO (A-174@LLZO) was carried out by using a mixture of methanol, acetic acid, and water. The A-174 silane molecules were mixed with methanol, acetic acid, and water mixture. The LLZO particles were then added to the mixture and were placed onto a hot plate for 3 hours at 80 °C with a stir bar. The solvent was then removed, and the particles were rinsed with isopropanol and centrifuged three times. Following the final centrifuge and rinsing, the particles were then dried under vacuum for 72 hours.

Composite polymer electrolytes were made by mixing PEO, LiTFSI, and 20 wt% TEGDME in ACN. The PEO–LiTFSI–20 wt% TEGDME mixture was stirred overnight with a stir bar or until completely dissolved. All fillers were dispersed under identical conditions, including extended mixing (12 h), to promote homogeneous particle distribution. The PEO concentration was maintained at 6 wt% (PEO : Li ratio = 15 : 1), and nanoparticles were added at 20 wt% relative to the PEO content. To evaluate the influence of filler type on the composite electrolyte performance, the gravimetric loading was fixed at 20 wt%. Due to the lower density of Al_2O_3 (~3.9 g cm^{-3}) compared to LLZO (~5.1 g cm^{-3}), the Al_2O_3 containing composites correspond to a higher filler volume fraction. Once the mixture of PEO–LiTFSI–

20 wt% TEGDME–20 wt% NPs was fully dissolved, the membrane was drop casted onto a flat sheet of Teflon. Membranes were visually inspected after casting, and any films exhibiting visible agglomeration were discarded and remade to ensure consistent dispersion quality across all samples. The observed particle distribution is consistent with the improved interfacial contact and ionic transport behavior discussed in the electrochemical analysis. The membrane was left to dry under vacuum at room temperature for 2–3 hours, or until completely dry. Once the membrane was dried, the Teflon was then folded in half and cut into discs with an area of roughly 1.2 cm^2. The thickness of the cast composite electrolyte membranes was measured from cross-sectional SEM images and found to be approximately ∼70 μm (±20 μm). As these membranes were made *via* drop-casting, total thickness control was not possible for this specific paper.

Computational methodology

We carried out spin-polarized Density Functional Theory (DFT) calculations for an Al-doped LLZO surface modified using the two silane-coupling agents investigated experimentally: methacryloxypropyl trimethoxysilane (A-174) and 3-aminopropyl triethoxysilane (APTES). The initial cubic phase LLZO structure of space group la–3d was sourced from the Crystallography Open Database (COD),[53–55] with lattice parameters: $a = b = c =$ 12.97 Å and $\alpha = \beta = \gamma = 90°$. A supercell consisting of 376 atoms was constructed using VESTA,[56] with a stoichiometry corresponding to the structure used in the experimental investigations, *i.e.*, $Li_{6.25}Al_{0.25}La_3Zr_2O_{12}$. A slab was created by applying a vacuum of 15 Å along the *c* direction in the bulk supercell. This slab was used as a simplified reference to approximate a general, bulk-like local coordination environment of a nanoparticle. The geometry of Al-doped c-LLZO structure was optimized using the Vienna *Ab Initio* Simulation Package (VASP).[57–59] The Projector-Augmented Wave (PAW) potentials for the elements were implemented as supplied by VASP.[57,60] To account for the exchange–correlation energies, we adopted the Generalized Gradient Approximation (GGA), based on the Perdew–Burke–Ernzerhof approach.[61] The kinetic energy cutoff was set to 600 eV to enhance accuracy, and the Brillouin zone was sampled at the gamma point with the *k*-mesh set based on the respective lattice parameters, *i.e.*, a = 12.97 Å; b = 25.95 Å; c = 30.97 Å. The energy convergence thresholds for the electronic self-consistent loop and ionic relaxation loop were set to 0.01 meV Å^{-1}, and 0.1 meV Å^{-1} respectively. All the structures were visualized using VESTA.[56]

A study on the mPEO-TMS(3-[methoxy(polyethyleneoxy)$_{6-9}$ propyl]tri-methoxysilane) modified $Li_{10}GeP_2S_{12}$ nanoparticle in Ref. 62 highlights that Si in mPEO-TMS forms strong bonds with the S in LGPS, to protect the nanoparticle from potential decomposition at the Li anodes and active cathode surfaces.[62] This reaction showed that three molecules of Li–OCH_3 are released upon formation of the SiS_3 bond. Adopting a similar mechanism for the investigation in this paper, we propose that Si forms three bonds with oxygen, *i.e.*, SiO_3, while releasing three molecules of Li–"alkyl group". This reaction is outlined in Fig. 1. The APTES modified structure produces three molecules of Li–OC_2H_5, whereas the A-174 modified structure yields three molecules of Li–OCH_3. The mechanism for an A-174 modified surface in the presence of protons derived from a protic solvent was also investigated.

Electrochemical measurements

All electrochemical measurements were done on a Biologic VSP300 potentiostat in a temperature-controlled chamber (ESPEC). The composite polymer electrolytes were placed between 0.9 cm^2 Li foil electrodes that were freshly polished. The Li metal and electrolyte were then assembled in a 2032-coin cell, with a 1.0 mm stainless steel spacer and wave spring; all cell parts were 304 stainless steel. Each experiment tested three cells, and the results shown in each figure represent the average of the three tested cells. No dedicated electrochemical formation cycle was performed prior to testing. Instead, cells were thermally conditioned during Arrhenius conductivity measurements (5–70 °C), followed by cooling to 20 °C and reheating to 60 °C. The cells were then held at 60 °C for 2 hours prior to further measurements. Potentiostatic electrochemical impedance (PEIS) measurements were performed with a 7 MHz to 1 or 0.1 Hz frequency range, 0.0 V *versus* the open circuit DC bias, 10 mV amplitude AC sine wave, and 20 points per decade sampling. Chronoamperometry was performed at +50 mV bias for 1000 s with 1 mV per 1 second sampling intervals to capture accurate currents. All electrochemical measurements were performed on at least n = 3 independently assembled cells per composition, with some samples tested in additional replicates to confirm reproducibility.

The bulk electrolyte resistance (R_b) was determined from the high-frequency intercept of the Nyquist plot with the real axis. Specifically, ionic conductivity (σ) was calculated using $\sigma = L/(R_b \times A)$, where L is the electrolyte thickness (∼70 μm) and A is the electrode area (0.9 cm^2). Temperature-dependent conductivity was analyzed using the Arrhenius relationship. At sufficiently high frequencies, interfacial processes cannot respond to the applied perturbation, and the measured impedance is therefore dominated by the bulk electrolyte resistance. At lower frequencies, interfacial contributions from the Li/electrolyte interface appear as a well-defined semicircle, followed by a low-frequency diffusion tail. Accordingly, the extracted R_b reflects the bulk electrolyte resistance with minimal contribution from interfacial impedance. This approach is consistent with established impedance analysis methods, where the bulk resistance is obtained from the high-frequency intercept prior to the onset of interfacial processes.[63] The separation between R_b and R_{int} values (Fig. S1) further supports the distinction between bulk and interfacial contributions.

To calculate the transference numbers, the Bruce–Vincent method was used because it is an accessible method that can distinguish ionic movement due to Li$^+$ from total ionic movement. Specifically, in CPEs, the Bruce–Vincent method is particularly suitable because it captures the complex ion transport behavior arising from both the polymer matrix and the in-

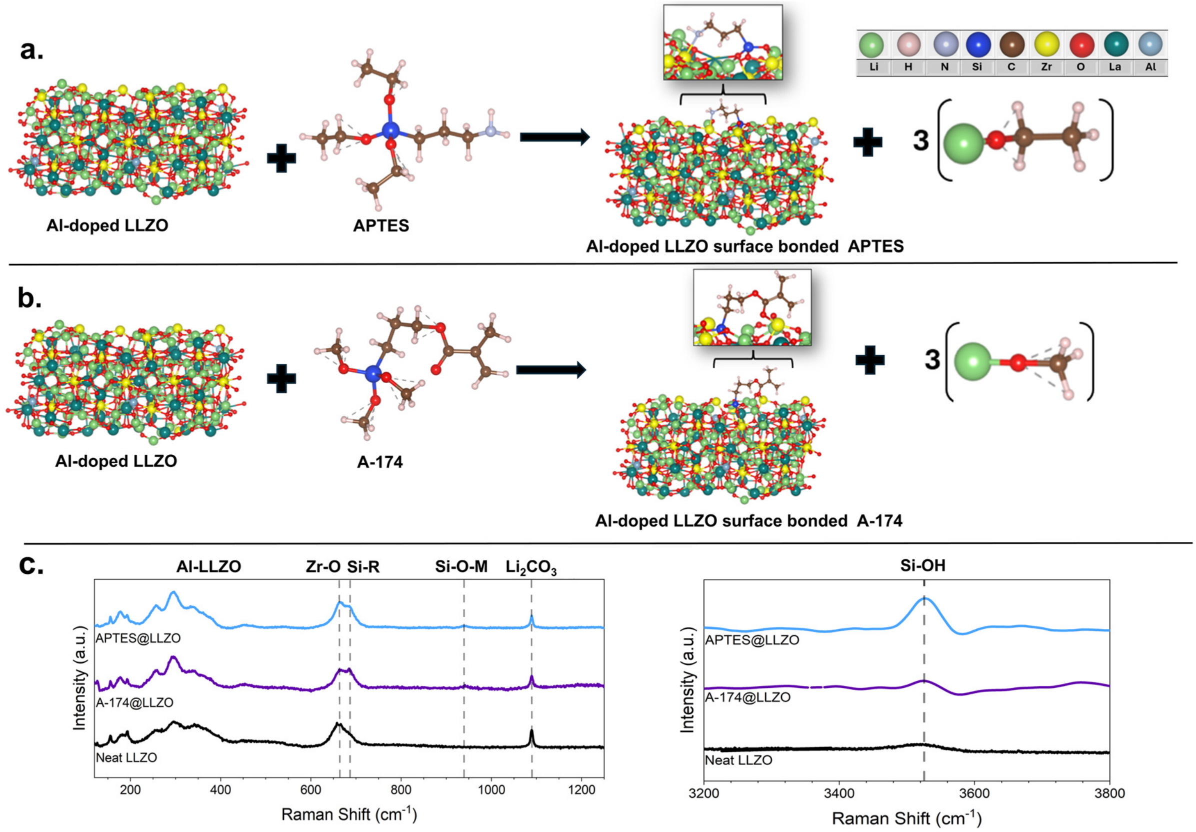

Fig. 1 LLZO surface modification (a) reaction of 3-aminopropyl triethoxysilane (APTES) and the Al-doped LLZO nanoparticles. The products are the silane-coupling agent bonded to the surface of Al-doped LLZO nanoparticle and three molecules of $LiOC_2H_5$. (b) Al-doped LLZO reaction with Methacryloxypropyl trimethoxysilane (A-174). The products are the A-174 bonded to the surface of the Al-doped LLZO nanoparticle and three molecules of $LiOCH_3$. (c) Raman spectra measured in two ranges: 200–1200 cm^{-1} and 3200–3800 cm^{-1}. Characteristics peaks are highlighted with grey dotted lines and assigned.

organic fillers. By using a Li symmetric cell, the method reflects the true electrochemical environment of the electrolyte during operation, including the interfacial dynamics between Li metal and the CPE. The steady-state polarization approach effectively distinguishes between the initial mixed ionic current and the predominantly Li^+ current after anion migration becomes suppressed, making it valuable diagnostic for quantifying Li^+ mobility in solid and semi-solid CPE systems. The Bruce Vincent equation is listed below:

$$t_{\mathrm{Li}} = \frac{I_{\mathrm{ss}}(\Delta V - i_0 R_0)}{I_0(\Delta V - i_{\mathrm{ss}} R_{\mathrm{ss}})}$$

The i_0 and i_{ss} are the initial and steady-state currents from the chronoamperometry results. The ΔV is the applied potential, also known as the bias voltage. The R_0 and R_{ss} values are the initial and steady-state resistance values. To ensure consistency, other established methods for determining the transference number were applied for comparison. The corresponding results are in SI Fig. S2, along with representative chronoamperometry profiles in Fig. S3.

Critical current density (CCD) measurements were performed using a staircase protocol in which the current density was increased in 20 μA cm^{-2} increments until short circuit. This approach probes dendrite penetration resistance under progressively increasing current densities rather than simulating continuous lithium deposition. Although the lithium plated during each individual step is small (~0.017 μm at 20 μA cm^{-2} for 10 min), the cumulative capacity passed prior to failure is substantially larger. This cumulative response provides a more representative measure of electrolyte stability under repeated plating conditions.

Solid-state NMR

All solid-state NMR experiments were performed on a Bruker Avance 3 console operating at a ^1H Larmor frequency of 400 MHz and equipped with a 1.9 mm HXY NMR probe. The spectrometer was controlled using TopSpin 3.7.0 software running on the Alma 9 operating system. The three samples tested by solid-state NMR were neat LLZO nanoparticles, A-174@LLZO nanoparticles, and APTES@LLZO nanoparticles, measured in the absence of polymer and lithium salt. One-dimensional ^1H static spectra were carefully acquired to quantify the proton content in each sample using identical acquisition parameters. To this end a Hahn echo pulse sequence

(90°–τ–180°–τ–acquire) was employed with an inter-pulse delay (τ) of 20 μs. The 90° pulse length was 3.1 μs at a power level of 13.1 W. Each spectrum was collected with 16 scans, a spectral width of 200 kHz, and an acquisition time of 20 ms. The receiver gain was set to 32 for all experiments. Sample masses were carefully determined using tared rotors to enable accurate scaling of spectra based on sample mass. We chose to use the Hahn echo sequence to improve baseline quality by an accurate first point determination of the FID and to help minimize background ^{1}H signal through phase cycling. The phase cycle employed was: ph1 = 0 1 2 3 0 1 2 3 (first pulse), ph2 = 1 2 3 0 3 0 1 2 (second pulse), and ph31 = 0 1 2 3 0 1 2 3 (receiver). Note how ph2 minus ph1 shifts by 180 degrees in the last four steps relative to the first 4 steps as this helps to subtract out background signal. One-dimensional ^{6}Li NMR spectra were acquired under magic angle spinning (MAS) at a spinning frequency of 20 kHz. A rotor synchronized single pulse experiment was used with a pulse length of 6.5 μs at 80 W. Each spectrum was recorded with 32 scans, a spectral width of 5 kHz, an acquisition time of 400 ms, and a recycle delay of 120 s. No ^{1}H decoupling was applied during acquisition.

Longitudinal relaxation (T_1) measurements for ^{7}Li were performed using a saturation recovery pulse sequence under MAS conditions at a spinning frequency of 20 kHz. The saturation block consisted of 200 loops of a 90° pulse (2.1 μs at 14 W) followed by a 5 ms delay. Following saturation, 48 recovery delays ranging from 1 ms to 200 s (spaced exponentially) were employed. Detection used a 90° pulse (2.1 μs at 14 W) followed by signal acquisition for 8.2 ms with a spectral width of 62.5 kHz. Eight scans were collected for each recovery delay with a recycle delay of 3 s between transients. No ^{1}H decoupling was applied during acquisition.

All NMR spectra were initially processed in TopSpin and subsequently exported as text files for further analysis. Custom C++ routines were developed for all subsequent data manipulation and fitting procedures. The ^{1}H spectra were scaled according to the measured sample mass to determine relative proton populations across samples. Saturation recovery data were integrated and fit to a bi-exponential relaxation model. Uncertainties in fitted parameters were estimated using the jackknife resampling algorithm.

Results and discussion

Mechanistic study of LLZO surface modification

To elucidate how silane surface chemistries influence LLZO reactivity and interfacial stability within CPEs, we first examined the fundamental interactions between each silane and the LLZO surface using density functional theory (DFT). These calculations establish the molecular-level framework needed to interpret subsequent electrochemical and spectroscopic trends. Two surface reactions were evaluated for Al-doped cubic LLZO modified with either APTES or A-174 under solvent environments matching experimental conditions (aprotic for APTES, protic for A-174). We first considered the surface reactions shown in Fig. 1a and b, in which Al-doped LLZO reacts directly with each silane coupling agent. Both reactions are endergonic and yield a SiO_3 anchoring bond to the LLZO surface. For APTES, the non-silicon terminus forms a Zr–N bond (bond length = 2.60 Å), whereas A-174 forms a Zr–O bond (bond length = 2.35 Å) at its non-silicon end (Fig. S4). Formation of the APTES-coupled LLZO surface requires 1.19 eV and releases three $LiOC_2H_5$ molecules. In contrast, forming the A-174 coupled surface requires 2.57 eV and produces three $LiOCH_3$-an energy cost, ~1.38 eV higher than the APTES reaction.

Raman spectroscopy was utilized to probe the crystalline lattice structure and verify successful surface functionalization. Spectra of neat LLZO, APTES@LLZO, and A-174@LLZO are shown in Fig. 1c. The low frequency region below ~500 cm^{-1} corresponds to the lattice vibrations of La and Li, providing a signature of cubic LLZO symmetry. The presence and positions of these peaks in all samples indicate that the cubic framework of LLZO is preserved after silane modification. The Zr–O lattice mode at ~660 cm^{-1}, another hallmark of cubic phase stability, remains unchanged in both modified samples, further confirming structural integrity.

Successful surface functionalization is evidenced by new vibrational modes corresponding to the silane coupling agents. Specifically, the appearance of the Si–R band (where R is the organic chain), is observed at ~690 cm^{-1} in the functionalized spectra. A magnified view of the Zr–O region, alongside the new Si–R bond, is provided in Fig. S5a. Further evidence of surface attachment is provided by the prominent band at ~940 cm^{-1}, which corresponds to the asymmetrical stretching of the Si–O–M bond (where M represents Zr or La from the LLZO surface), indicating the formation of the silane-LLZO bond. This Li_2CO_3 signal, along with the characteristic N–H bending/deformation modes (from the APTES amino group) around ~1450 cm^{-1}, is highlighted in the magnified Fig. S5b. The complete spectrum confirms the organic component of the silanes, with stretching modes for the alkyl C–H groups clearly visible in the region of ~2900–3000 cm^{-1} (Fig. S5c). Finally, the broad peak at ~3500 cm^{-1} is attributed to surface Si–OH groups.

Minor impurities are also observed in the spectra. All LLZO samples exhibit a peak near ~1090 cm^{-1} corresponding to Li_2CO_3, with smaller intensity in the modified samples, suggesting partial mitigation of surface carbonate during functionalization. A weak feature around ~300 cm^{-1}, which has been previously attributed to $La_2Zr_2O_7$ formation, is also present and appears slightly more pronounced after silanation. While the bulk cubic LLZO structure is retained, the appearance of these minor phases may contribute to observed Li loss and changes in local lithium environments, highlighting the importance of starting material purity and careful surface treatment. Overall, the Raman data confirm that silane functionalization modifies the LLZO surface without significantly disrupting the cubic lattice, while also revealing the presence of minor secondary phases that could influence lithium content and mobility.

Having established through both DFT and Raman spectroscopy that APTES and A-174 generate distinct anchoring chemistries on the LLZO surface while preserving the cubic framework, we next examined how the surrounding chemical environment influences these reactions. Our previous study[45] showed that achieving a stable APTES@LLZO interface requires strictly aprotic, moisture free conditions to prevent Li^+/H^+ exchange, which disrupts the cubic LLZO structure and lowers conductivity. APTES is effective because its silane end forms the bond to the LLZO surface, while the amine ($-NH_2$) group provides a Lewis-basic coordination site that suppresses Li_2CO_3 formation and facilitates Li^+ hopping from the ceramic into the polymer matrix. In contrast, A-174 lacks an amine functionality and instead contains a methacrylate group. Although the methacrylate does not coordinate Li^+, it enables formation of a 'chemical bridge' between the LLZO surface and the PEO-based polymer: the methacrylate can participate in secondary interactions and light cross-linking with nearby polymer chains, improving interfacial adhesion and enhancing ceramic–polymer contact.

Consequently, the A-174 synthesis intentionally employs a mildly acidic protic solvent, which is necessary to promote the reaction between the A-174 silane and the LLZO surface, with conditions carefully controlled to minimize lithium hydroxide formation and structural degradation, while strengthening contact. Crucially, the retention of the strong, single Zr–O peak and the simple low frequency modes in the A-174@LLZO Raman spectrum confirms that carefully controlled mildly acidic protic solvent conditions did not cause structural decomposition or conversion of the LLZO cubic phase.

To further understand how the protic environment influences the interfacial chemistry of A-174 on LLZO, we evaluated how protons interact with the silane-modified surface using DFT calculations. APTES functionalization was carried out in an aprotic solvent; hence, no protons were considered. We first carried out calculations of the proton reacting with the A-174 coupled LLZO structure to determine the silane's influence on the protonation process. Protonation was evaluated at two distinct positions (Fig. S6): (i) a site further from the forming SiO_3 bond, and (ii) a site closer to the Si atom. In both cases, proton attack leads to substitution of a surface Li^+ ion and its subsequent release, consistent with the experimentally observed sensitivity of LLZO to acidic environments. The reaction is more exergonic when the protonation occurs farther from the SiO_3 site ($dE = -6.03$ eV) compared to protonation adjacent to the SiO_3 bond ($dE = -2.25$ eV), indicating a preferred pathway for proton-induced Li^+ displacement on the A-174 modified surface. This large thermodynamic difference suggests that the presence of the A-174 silane disfavors proton-induced Li^+ displacement at the protected Si site, suggesting a steric or electronic hindrance effect.

We then compared the reaction of A-174 and LLZO in the presence of H^+ derived from the protic solvent (Fig. 2a) with the reaction described in Fig. 1a, the modification of APTES in an aprotic solvent. Two mechanisms were considered, with computed energetics presented in Fig. 2b. In the first mechanism, protonation and silanation occur consecutively, with an overall energy change of 0.32 eV (Fig. S7): the protonation step

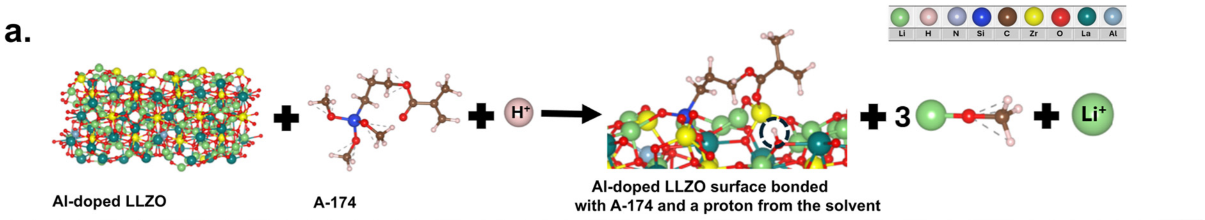

b.

	ΔE (eV)
3-Aminopropyl triethoxysilane (APTES) only APTES reacts with the surface	1.19
Methacryloxypropyl trimethoxysilane (A-174) only A-174 reacts with the surface	2.57
Methacryloxypropyl trimethoxysilane (A-174) proton and A-174 react with the surface in consecutive steps	0.32
Methacryloxypropyl trimethoxysilane (A-174) proton and A-174 react with the surface simultaneously	-0.01

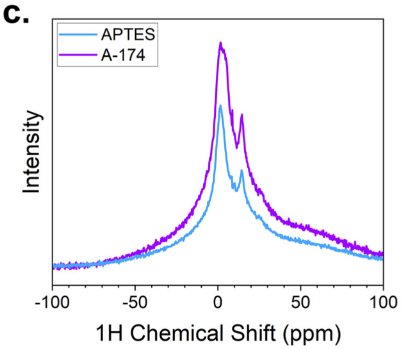

Fig. 2 Mechanistic study of LLZO surface modification (a) modification of the surface of Al-doped LLZO nanoparticles by the simultaneous addition of A-174 silane and the proton obtained from the protic solvent (the protic solvent includes methanol, acetic acid, and water). (b) Outlines the quantitative values of the energy change for each specific reaction. The first two rows are the change in energy associated with the functionalization of LLZO with APTES (top row) and A-174 (second row). The bottom two rows account for the protic solvent used with A-174, with the third row demonstrating the consecutive steps where the proton from the protic solvent reacts with the surface of LLZO nanoparticles first, followed by the addition of A-174 silane. The last row represents the reaction depicted in a, where the silane and the proton from the protic solvent react with the surface simultaneously, resulting in a change in energy of −0.01 eV. (c) Solid-state nuclear magnetic resonance spectra, showing the relative number of protons in both the A-174 and APTES modified nanoparticles.

is highly exergonic (dE = −3.78 eV), while the subsequent reaction of the protonated surface with A-174 is highly endergonic (dE = 4.09 eV), indicating that silanation may be unfavorable if the LLZO surface becomes protonated before the silane addition. In the second mechanism, protonation and silanation occur simultaneously, with an overall dE of −0.01 eV, suggesting that this pathway is thermodynamically more feasible. While these calculations do not directly predict Li^+ transport kinetics, they indicate that A-174 functionalization in a protic solvent is less prone to proton-induced Li^+ displacement, potentially maintaining Li^+ availability at the interface. Comparison of A-174 functionalization in protic *versus* aprotic solvents highlights the role of solvent: the reaction is more favorable under protic conditions (dE = −0.01 eV) than under aprotic conditions (dE = 2.57 eV), emphasizing the importance of solvent choice in controlling interfacial chemistry.

It is important to note that, in the absence of high-temperature pretreatment, LLZO surfaces are likely terminated with hydroxyl (–OH) species (*e.g.*, LiOH or adsorbed moisture-derived species). As a result, silane functionalization may proceed *via* condensation with these surface hydroxyl groups, involving proton exchange rather than direct Li^+ displacement. In the present computational model, the proton participating in the reaction is derived from the protic solvent; however, under experimental conditions, both solvent and surface hydroxyl species may serve as proton sources, enabling a concerted silanation pathway. While this represents an alternative reaction pathway, the resulting Si–O–surface bonding and interfacial modification remain consistent with the mechanism proposed here. Notably, the present analysis is centered on changes in Li chemical environments, as will be discussed in detail through ^{6}Li NMR and corresponding modeling; therefore, proton-mediated surface processes are not explicitly resolved in this framework.

To experimentally probe the local environments implicated in the proposed silanation mechanisms, solid-state ^{1}H NMR was performed on both APTES@LLZO and A-174@LLZO nanoparticles. As shown in Fig. 2c, the APTES@LLZO sample exhibits a lower overall ^{1}H NMR signal intensity relative to A-174@LLZO. Comparison with neat LLZO (Fig. S8), which shows the highest signal, indicates that much of the ^{1}H signal arises from surface hydroxyl groups and adsorbed moisture present on the unmodified particles. The A-174 modification, carried out in a protic solvent, introduces additional proton-containing species such as residual solvent or solvent-surface interactions, resulting in a higher ^{1}H intensity than the APTES sample. In contrast, APTES@LLZO, prepared under strictly aprotic conditions, does not introduce additional protons, and the lower intensity relative to neat LLZO likely reflects partial replacement or coverage of surface hydroxyl groups during silanization. We note that these ^{1}H signals may arise from distinct chemical environments (surface OH vs residual solvent vs silane groups) and are not necessarily equivalent, so intensity differences reflect changes in local proton environments rather than absolute proton content. Taken together, the DFT calculations and ^{1}H NMR evidence indicates that both A-174 and APTES functionalization preserve the cubic LLZO framework while altering the local proton environment, setting the stage to evaluate how these distinct surface chemistries influence the electrochemical behavior of inert and Li-active nanoparticle composites.

Electrochemical evaluation of surface modification of nanoparticles

Having established the molecular-level modification of the LLZO interface through A-174 and APTES functionalization, we next assessed how distinct surface chemistries influence the macroscopic electrochemical performance of the CPEs. Key parameters, including ionic conductivity, transference number, and critical current density (CCD), provide insight into the interplay between surface chemistry, interfacial transport, and dendrite suppression. The CCD is used here as comparative metric to evaluate lithium deposition stability under applied current, rather than as a direct measure of intrinsic ion-conduction behavior. Among these, CCD is especially informative as it quantifies the maximum current the electrolyte can sustain before short-circuiting occurs, reflecting both mechanical and electrochemical stability at the lithium–metal interface. Higher CCD values indicate that the system can operate at greater current densities – essential for fast charging – without compromising safety or performance. PEO–LiTFSI electrolytes are thin and mechanically weak, making CCD especially sensitive to the incorporation of additives.

The neat PEO–LiTFSI–20 wt% TEGDME electrolyte exhibited a CCD of 160 μA cm^{-2} (Fig. 3a), the lowest measured value, consistent with its lack of mechanical reinforcement and inability to effectively suppress dendrite formation. Incorporation of LLZO nanoparticles with distinct silane modifications led to notable differences in CCD. APTES@LLZO produced a CCD of 200 μA cm^{-2}, while A-174@LLZO more than doubled this value to 420 μA cm^{-2} (Fig. 3b and c). The substantially higher CCD of A-174@LLZO highlights the combined benefit of Li-active nanoparticles and favorable silane-induced interfacial interactions in stabilizing lithium deposition, motivating further focus on this system in subsequent experiments. Notably, the A-174@LLZO sample sustained 0.77 mAh cm^{-2} before short circuit, corresponding to ∼3.73 μm of cumulative lithium displacement.

To decouple the contributions of the nanoparticle bulk from surface chemistry, 500 nm aluminum oxide (Al_2O_3) nanoparticles were incorporated as a non-Li-containing, inert analogue of LLZO. The PEO–LiTFSI–20 wt% TEGDME–20 wt% Al_2O_3 system ("neat Al_2O_3") exhibited a CCD of 300 μA cm^{-2} (Fig. 3d), indicating that the presence of bulk nanoparticles alone can enhance interfacial stability, likely through mechanical reinforcement. Interestingly, when Al_2O_3 was modified with silane A-174 (A-174@Al_2O_3), the CCD decreased to 220 μA cm^{-2} (Fig. 3e). The reduced CCD suggests that surface chemistry alone does not necessarily improve – and even may compromise – performance for inert particles, possibly by interfering with favorable polymer–particle interactions. Complementary PEIS measurements recorded during CCD

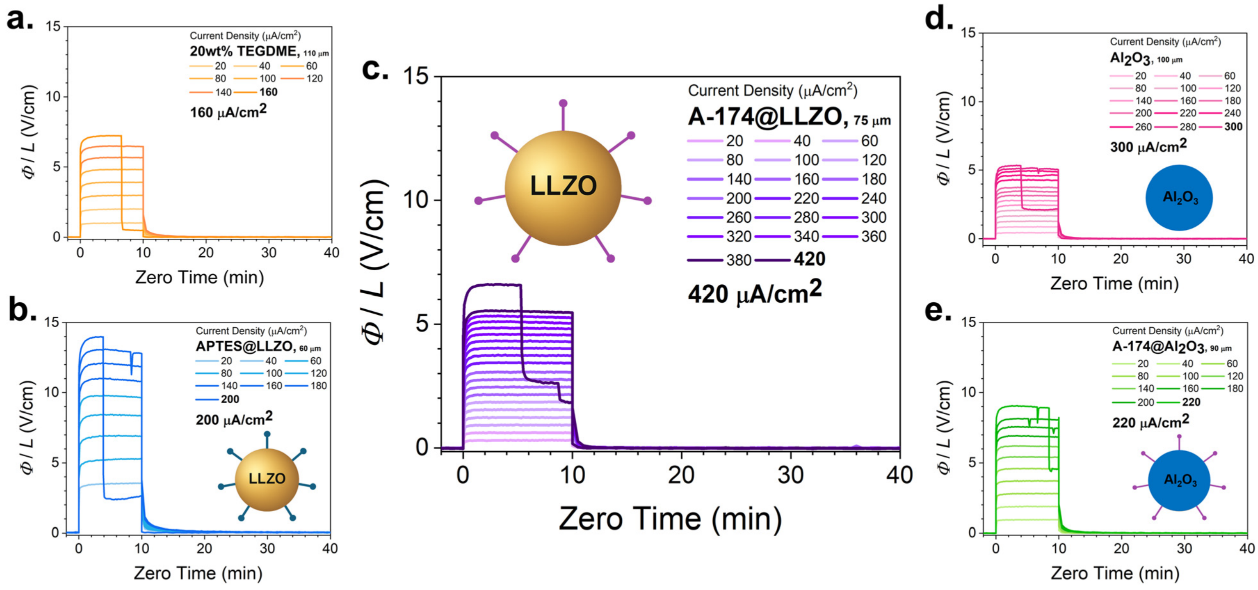

Fig. 3 Galvanostatic lithium plating on various composite electrolyte membranes (a) 20 wt% TEGDME added to the PEO–LiTFSI matrix. (b) APTES@LLZO (c) A-174 @LLZO (d) Al_2O_3 nanoparticles with no modifications. (e) A-174 modified Al_2O_3 particles, each plot displays voltage normalized to thickness (ϕ/L) *versus* time, with increasing current densities applied stepwise until shorting. Cartoon inserts represent the filler particle type and surface chemistry.

testing (Fig. S9) corroborate the observed short-circuit events, providing additional confirmation of the relative performance of each system. Collectively, these measurements demonstrate that both the surface chemistry and the nature of the incorporated nanoparticle influence CCD. While ionic conductivity remains comparable across samples, differences in CCD correlate more strongly with variations in interfacial resistance, indicating that nanoparticle surface functionalization primarily enhances interfacial transport and stability, rather than bulk ion conduction. This motivates a more detailed analysis of ionic conductivity and transference number.

Effect of Surface modification of nanoparticles on lithium transport

While CCD captures the mechanical and electrochemical limits of the electrolyte under high-rate operation, a complete understanding of electrolyte performance also requires assessing properties that govern steady-state ion transport. We therefore next examine the ionic conductivity, lithium-ion transference number, and interfacial resistance of each composite to determine how nanoparticle type and surface functionalization influence fundamental transport behavior. A comparison of the neat PEO–LiTFSI electrolyte with the formulation containing 20 wt% TEGDME reveals a substantial increase in ionic conductivity upon TEGDME addition (Fig. S10). However, incorporating nanoparticles – whether inert or Li-active – does not produce further increases beyond this TEGDME-driven enhancement, as shown in the Arrhenius plot (Fig. 4a) and the corresponding 60 °C values (Fig. 4b). Complementary conductivity and PEIS data collected at 30 °C are provided in Fig. S11. Across the nanoparticle-containing systems, the conductivities were largely comparable within error, with both Al_2O_3-based composites and A-174@LLZO clustering near the TEGDME-only formation. The only clear deviation was observed for APTES@LLZO, which exhibited consistently lower conductivity. While neat PEO–LiTFSI is included as a reference for intrinsic transport properties (ionic conductivity and transference number), the addition of TEGDME is necessary to obtain a more amorphous, well-wetted polymer matrix that enables stable and reproducible electrochemical measurements. This distinction is particularly important when evaluating interfacial transport phenomena. Importantly, TEGDME is present at the same concentration in all samples studied; therefore, it does not account for differences in electrochemical performance, which are instead attributed to variations in nanoparticle chemistry and surface functionalization. Notably, prior studies have shown that the incorporation of unmodified LLZO into PEO–LiTFSI can reduce ionic conductivity relative to the neat polymer, despite the high intrinsic conductivity of LLZO, due to interfacial limitations associated with surface impurities and poor compatibility.[33] Accordingly, surface functionalization is employed here to mitigate these effects and enable a more meaningful assessment of polymer–particle interfacial transport.

To build a more complete picture of ion transport in these composites, we next examine the lithium-ion transference number (t_+), which reflects the fraction of total ionic current carried by Li^+. Fig. 4c shows transference numbers calculated using the Bruce–Vincent method, while Fig. S2 presents six additional calculation approaches along with the corresponding chronoamperometry data (Fig. S3) used to extract absolute transference numbers in CPEs. We note that while

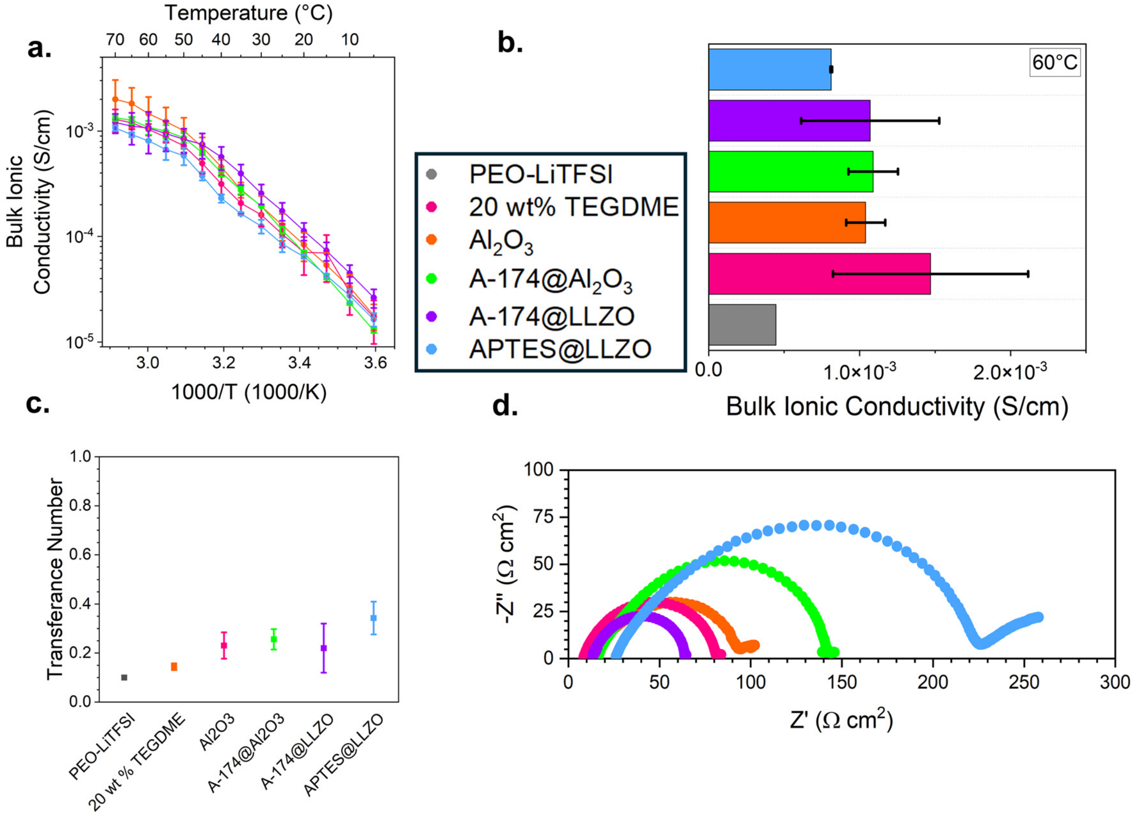

Fig. 4 Electrochemical characterization of Li-transport. (a) Bulk ionic conductivity graph with error bars. (b) Ionic conductivity values at 60 °C. (c) Average of the Bruce–Vincent transference number calculations, with error bars. (d) Potentiostatic electrochemical impedance spectroscopy (PEIS) measurements at 60 °C for each sample.

these values provide insight into relative trends, the derivations of the formulations do not fully capture the complex multi-phase nature of these CPE systems, and this absolute t_+ should be interpreted with caution. Collectively, the Bruce–Vincent derived averages suggest that Li^+ contributes roughly 25–33% of the total ionic conductivity in most samples, except for APTES@LLZO, which shows a higher t_+ of ~0.45. This trend indicates that while the addition of TEGDME and Li-active nanoparticles can enhance interfacial transport, the overall cation transport remains modest, highlighting the need to balance polymer flexibility, nanoparticle chemistry, and Li^+ mobility in CPE design.

PEIS measurements at 60 °C were used to evaluate interfacial and bulk resistances (Fig. 4d), complementing the ionic conductivity data. Prior to these measurements, cells were thermally conditioned during Arrhenius testing, and PEIS spectra collected during this process (Fig. S12 and S13) reveal an evolution in interfacial impedance, which stabilizes after the 2 hour isothermal hold. Consistent ionic conductivity trends observed during cooling and reheating cycles (Fig. S12) further indicate that a stable polymer–lithium interface is established prior to electrochemical testing. This behavior is characteristic of polymer electrolytes, where temperature-driven segmental motion can facilitate interfacial wetting and equilibrium. Among the samples, A-174@LLZO exhibited the lowest interfacial resistance at 65 $\Omega cm,^2$ whereas APTES@LLZO showed a significantly higher value of 228 Ω cm^2. Although the interfacial feature observed in Li/composite electrolyte/Li cells cannot be assigned exclusively to the internal PEO/LLZO interface, its magnitude is comparable to values obtained for PEO/LLZO interfacial resistance in separate planar-cell modeling studies. For the A-174-modified system, the reduced impedance likely reflects not only improved PEO/LLZO contact, which was the intended effect of the surface chemistry, but also an unexpected beneficial influence on the Li/composite-electrolyte interface.[64] While the nanofillers are embedded within the polymer matrix and do not directly contact the lithium electrode, A-174 functionalization leads to a measurable reduction in interfacial resistance. Surface modification proceeds through a concerted proton-assisted silanation pathway, in which protonation and silane attachment occur simultaneously. Computational analysis indicates that a sequential mechanism involving prior protonation of the LLZO surface is thermodynamically unfavorable, whereas the coupled pathway is energetically accessible. This reaction is enabled under protic conditions, where the proton participating in the concerted step is derived from the solvent; under experimental conditions, surface hydroxyl groups (such as Li_2CO_3 or absorbed –OH groups) may also serve as proton sources. The resulting organosilane-modified surface replaces inorganic surface species with more polymer-compatible functional groups, reducing interfacial mismatch within the CPE. This modification is consistent with the observed decrease in interfacial resistance and improved electrochemical performance, consistent with enhanced ion transport across polymer–filler interfaces. Additionally, surface functionalization may influence interphase formation at the lithium interface. Although the fillers are not directly exposed at the electrode surface, mobile species or interfacial reaction products derived from the functionalized surface may contribute to the formation of a more favorable interphase and reduced interfacial impedance, consistent with prior reports.[64]

These differences align with CCD trends, as higher interfacial resistance in APTES@LLZO corresponds to its lower CCD, while the low interfacial resistance of A-174@LLZO supports its higher current-carrying capacity. Bulk resistance values also mirror trends in ionic conductivity (Fig. 4b), with APTES@LLZO slightly higher than A-174@LLZO. The remaining samples – A-174@Al_2O_3, neat Al_2O_3, and 20 wt% TEGDME – exhibit intermediate interfacial resistances consistent with their respective CCDs. Specifically, the silanized Al_2O_3 particles exhibited higher interfacial resistance and correspondingly lower CCD, likely due to the surface-grafted organic layer immobilizing PEO chains at the filler surface, increasing local semi-crystallinity and suppressing the segmental motion required for Li^+ transport.[45,65] The interfacial polymer immobilization imposes an additional barrier to ion transfer, leading to elevated impedance. In contrast, A-174@LLZO delivers a higher CCD and lower interfacial resistance because the conductive LLZO backbone combined with A-174 coupling improves wetting and preserves fast-ion pathways at the filler–polymer interface, whereas the organic graft on Al_2O_3 forms a more resistive interfacial layer. Overall, these results suggest that incorporating a Li-active bulk particle with optimized surface functionalization, as in A-174@LLZO, reduces interfacial resistance consistent with enhanced Li^+ mobility at the interface, whereas TEGDME primarily enhances bulk conductivity without substantially impacting interfacial behavior.

To assess the impact of silane surface modifications on lithium dynamics within LLZO-based materials, ^6Li NMR was performed on neat LLZO, APTES@LLZO, and A-174@LLZO nanoparticle samples. Fig. 5a shows the ^6Li shift spectra, normalized to the integrated intensity of the neat LLZO (set to 1.0). The central peaks for all samples lie between 1.2–1.6 ppm, consistent with lithium in a diamagnetic, fast-ion-conducting environment typically associated with LLZO. Looking specifically at the chemical shift and integration trends, it is shown that neat LLZO exhibits the most intense signal. Then, APTES@LLZO shows a slight shift downfield to 1.2 PPM and retains 83% of the integrated intensity. A-174@LLZO shifts further downfield to 1.28 PPM, with the lowest relative intensity (72%). The downfield shifts observed in the silane modified samples suggest changes in the Li^+ environment, which may arise from bulk structural effects, such as partial formation of $La_2Zr_2O_7$ or other secondary phases during silanation, rather than surface-specific interactions. The reduction in Li is also shown in the silanated samples in Fig. 1a and b. In the reaction, there is a product of $LiOCH_3$ which was either eliminated from the sample during the silane cleaning process, or formed immobilized or NMR-

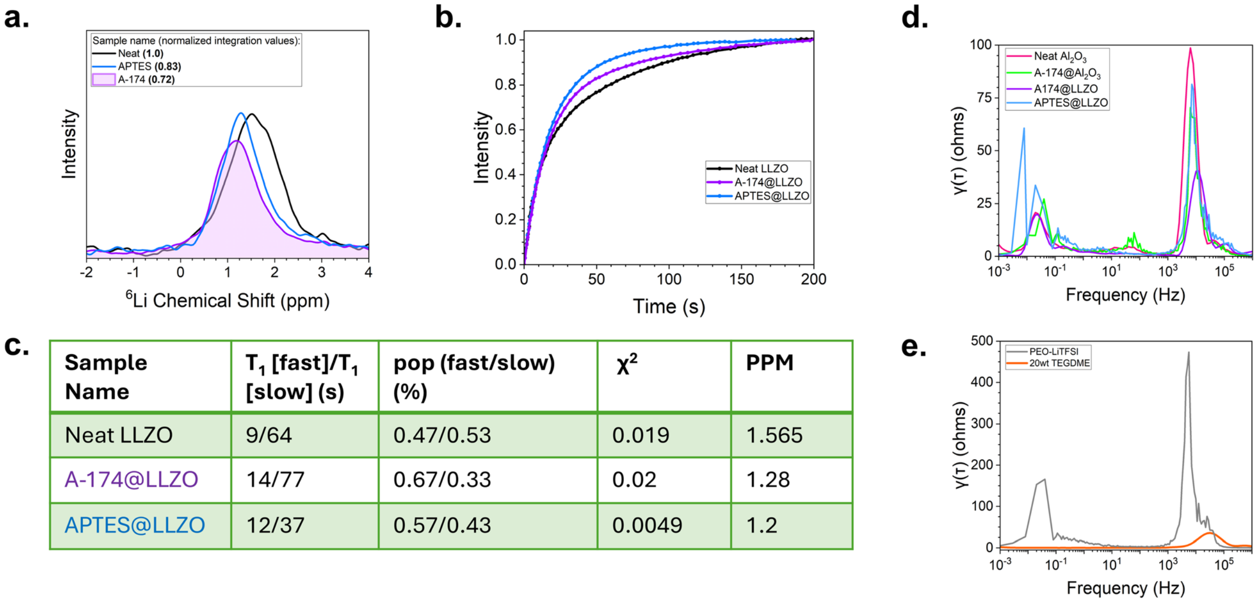

Sample Name	T_1 [fast]/T_1 [slow] (s)	pop (fast/slow) (%)	χ^2	PPM
Neat LLZO	9/64	0.47/0.53	0.019	1.565
A-174@LLZO	14/77	0.67/0.33	0.02	1.28
APTES@LLZO	12/37	0.57/0.43	0.0049	1.2

Fig. 5 Lithium transport kinetics. (a) Normalized ^6Li magic angle spinning (MAS) NMR spectra showing chemical shifts for neat LLZO, APTES@LLZO, and A-174@LLZO with the integration values shown in the legend, (b) T_1 relaxation curve obtained from saturation recovery measurements. (c) Extracted relaxation parameters from b. Including T_1 values for fast and slow components, the population fractions, χ^2 values, and the peak chemical shift (PPM) for each sample. (d) Distribution of relaxation time (DRT) graph showing frequency *versus* resistance values. (e) DRT graph for samples without nanoparticles.

invisible lithium species, which then resulted in a reduction of Li^+ content.

The mobility of Li^+ ions in each sample was further characterized by using ^6Li T_1 relaxation measurements. Relaxation dynamics were analyzed *via* biexponential fitting, revealing two lithium populations: a fast-relaxing component (T_1[fast]) and a slow-relaxing component (T_1[slow]), plotted in Fig. 5b. Reduced χ^2 values indicate good fits for all samples. Neat LLZO exhibits a roughly balanced population between fast and slow lithium environments, consistent with a mixture of more mobile and more localized Li^+ species. Both silane-modified samples increase the fraction of the fast-relaxing population relative to neat LLZO, with A-174@LLZO showing the largest fast fraction (67%) and APTES@LLZO slightly smaller (57%). In addition, APTES@LLZO displays a shorter T_1[slow] (37 s) compared to neat LLZO, which may reflect subtle differences in local Li^+ environments, such as heterogeneity or interactions with paramagnetic centers, rather than a direct measure of macroscopic ion mobility. Overall, the T_1 analysis demonstrates that silane functionalization modifies the distribution of lithium environments within LLZO, with A-174@LLZO showing the most pronounced changes in the fast-relaxing population. These local-scale differences in Li^+ dynamics are consistent with the electrochemical transport measurements presented earlier – namely, lower interfacial resistance and higher CCD – suggesting that surface chemistry can influence ion mobility at the particle interface and contribute to enhanced macroscopic transport.

Although the Al_2O_3-containing composites correspond to an increased volume fraction due to the lower density of Al_2O_3, this increased volume fraction would be expected to more strongly influence polymer matrix properties, including reduced segmental mobility, increased tortuosity, and potential changes in crystallinity. However, despite this greater degree of polymer disruption, the Al_2O_3-based composites exhibit inferior electrochemical performance of the LLZO–CPEs suggest that the intrinsic ionic properties of the filler dominate over simple volumetric effects. As shown in Fig. 5c, the ^6Li NMR T_1 relaxation data for the functionalized nanoparticles reveals a significant shift toward a fast-relaxation regime (T_1 = 12–14 s), accounting for 57–67% of the lithium population. This high surface mobility—most pronounced in the A-174@LLZO sample—indicates that the LLZO particles provide active, high-flux ion-transport pathways. In contrast, Al_2O_3 is an ionically insulating, passive filler that lacks these mobile lithium sites. Therefore, while Al_2O_3 may more significantly disrupt the polymer matrix due to its higher volume fraction, it simultaneously increases tortuosity without providing a compensatory conduction pathway. The correlation between the increased fast-relaxing lithium population and improved electrochemical performance indicates that filler surface chemistry, rather than volumetric loading, is the primary driver of transport behavior in these systems.

The distribution of relaxation times (DRT) graph shown in Fig. 5d and e demonstrates three major frequency regions. For this paper, the high frequency range is from 10^3 Hz to 10^5 Hz, which is the interfacial resistance values and grain boundary. The mid-frequency range is 10^0 Hz to 10^2 Hz, which is likely the interfacial continued, and the charge transfer resistance at the electrode/electrolyte boundary. The low-frequency range is from 10^{-3} Hz to 10^{-1} Hz, and this region is mass transport/diffusion. The uncertainty bands obtained *via* Monte-Carlo resampling of the fitted PEIS spectra are provided in Fig. S14. Looking specifically at the graph in Fig. 5d, there is a large peak in all samples in the high frequency range, which is the fastest and most resistive processes. The height of the main peak in this region directly reflects the quality of the solid electrolyte layer. For the neat Al_2O_3 sample, this curve has the highest and broadest peak, indicating the highest total resistance in the system, likely due to poor ion mobility or poor interface quality in this system. The next highest peak is APTES@LLZO and A-174@Al_2O_3, which are similar and both show a moderate peak in the same region as the neat Al_2O_3 sample. These values align with the PEIS graph shown in Fig. 4d. However, the A-174@LLZO line has a very small resistance value when compared to the other samples, and it also has this process occur at a higher frequency value, denoting that the A-174@LLZO modification is changing the time constant and speeding up the reaction. Looking at the lower frequencies, the A174@LLZO continues to have the lowest resistance values out of all the samples. APTES@LLZO has a very high mass transport/diffusion resistance value.

The complementary DRT and solid-state NMR analyses collectively demonstrate that A-174 surface functionalization significantly accelerates lithium transport kinetics in LLZO-based systems. In the DRT spectra, the A-174@LLZO sample exhibits a pronounced shift of the primary relaxation peak toward shorter times compared to neat LLZO, consistent with a reduction in interfacial resistance and faster charge transfer dynamics. This observation aligns with the NMR relaxation analysis, where biexponential fitting revealed an increased proportion of the fast-relaxing lithium population (67%) and higher T_1 values for both the fast and slow environments in A-174@LLZO. These results indicate that A-174 modification promotes more mobile or uniformly coordinated Li^+ species, likely through improved surface wetting and reduced interfacial inhomogeneity. In contrast, APTES@LLZO, while also increasing the fast-relaxing population (57%), displays a shorter T_1 (slow), suggesting a more heterogenous lithium environment. APTES@LLZO also does not have a shorter DRT time when compared to the Al_2O_3 samples. The correlation between the shorter DRT relaxation times and enhanced T_1 dynamics in A-174@LLZO confirms that silane functionalization effectively facilitates Li^+ mobility at both the bulk and interfacial levels. This enhanced ionic response is crucial for solid-state battery performance, as it translates to lower polarization, faster reaction kinetics, and improved long-term interfacial stability.

Conclusions

Overall, this study demonstrates that silane surface functionalization serves as an effective strategy to enhance the interfacial and transport properties of LLZO-based solid electrolytes. Among the silane modifiers investigated, A-174 functionalization yielded the most significant improvements across all electrochemical and spectroscopic metrics. The A-174@LLZO sample exhibited the highest critical current density, indicating improved interfacial stability and resistance to Li dendrite formation. Electrochemical impedance and DRT analyses further confirmed a substantial reduction in interfacial resistance and a shift toward shorter relaxation times, consistent with faster charge transfer kinetics at the Li/LLZO interface. Additionally, the A-174 modified sample showed the highest lithium-ion transference numbers, signifying more selective Li^+ transport within the composite. Solid-state ^6Li NMR relaxation analysis provided complementary insight into the origin of these improvements. Biexponential fitting of T_1 data revealed an increased population of fast-relaxing Li environments in A-174@LLZO, along with longer relaxation times for both fast and slow components, suggesting enhanced Li^+ mobility and a more homogeneous ionic environment. These findings support the conclusion that A-174 functionalization improves both bulk and interfacial ion dynamics by creating more uniform, less constrained Li pathways and improving contact at the solid-state interface. Overall, the integration of electrochemical and spectroscopic analyses highlights the critical role of surface chemistry in enabling lithium-ion transport. The A-174 silane modifier effectively bridges the mechanical and chemical mismatch between the LLZO surface and polymer matrix, resulting in faster interfacial kinetics and improved electrochemical stability. This work establishes a clear structure–property relationship between silane functionality and ion transport, providing a practical framework for interface design. By carefully selecting nanofiller type and optimizing surface chemistry, we can further improve this design framework with the long-term aim of enabling continuous bulk transport through Li-containing nanofillers for a high-performance solid-state electrolyte.

Conflicts of interest

There are no conflicts to declare.

Data availability

The data that support the findings of this study are available from the corresponding author upon reasonable request.

Supplementary information (SI) is available. See DOI: https://doi.org/10.1039/d6eb00043f.

Acknowledgements

This work was funded by the U. S. Department of Energy, Office of Critical Materials and Energy Innovation (CMEI), Office of Energy Efficiency and Renewable Energy (Grant# VT1201000), with support from Thompson, S. T. and Duong, T. Research was carried out at Argonne National Laboratory which is supported by the USA. Department of Energy, Office of Science, Office of Basic Energy Sciences, under contract no. DE-AC0206CH1135. J. C. was supported as part of the Energy Storage Research Alliance "ESRA" (DE-AC02-06CH11357), an Energy Innovation Hub funded by the U. S. Department of Energy, Office of Science, Basic Energy Sciences. Authors gratefully acknowledge the computing resources provided on Improv and Bebop, high-performance computing clusters operated by the Laboratory Computing Resource Center at Argonne National Laboratory. The views expressed herein do not necessarily represent the views of the U. S. Department of Energy or the United States Government. The authors also thank Kaline Nascimento da Silva for assisting with Raman measurements, and Benjamin Ketter for help with distribution of relaxation times (DRT) analysis. The authors acknowledge the use of artificial intelligence-assisted tools for generation of the Table of Contents graphic and for language refinement. These tools were used solely for visualization and editorial purposes; all scientific analysis, interpretation, and conclusions are the responsibility of the authors.

References

1 P. Bonnick and J. Muldoon, The Quest for the Holy Grail of Solid-State Lithium Batteries, *Energy Environ. Sci.*, 2022, **15**(5), 1840–1860, DOI: 10.1039/D2EE00842D.

2 P. Albertus, V. Anandan, C. Ban, N. Balsara, I. Belharouak, J. Buettner-Garrett, Z. Chen, C. Daniel, M. Doeff, N. J. Dudney, B. Dunn, S. J. Harris, S. Herle, E. Herbert, S. Kalnaus, J. A. Libera, D. Lu, S. Martin, B. D. McCloskey, M. T. McDowell, Y. S. Meng, J. Nanda, J. Sakamoto, E. C. Self, S. Tepavcevic, E. Wachsman, C. Wang, A. S. Westover, J. Xiao and T. Yersak, Challenges for and Pathways toward Li-Metal-Based All-Solid-State Batteries, *ACS Energy Lett.*, 2021, **6**(4), 1399–1404, DOI: 10.1021/acsenergylett.1c00445.

3 D.-H. Liu, Z. Bai, M. Li, A. Yu, D. Luo, W. Liu, L. Yang, J. Lu, K. Amine and Z. Chen, *Developing High Safety Li-Metal Anodes for Future High-Energy Li-Metal Batteries: Strategies and Perspectives*, 2020. DOI: 10.1039/C9CS00636B.

4 S. Kim, G. Park, S. J. Lee, S. Seo, K. Ryu, C. H. Kim and J. W. Choi, Lithium-Metal Batteries: From Fundamental Research to Industrialization, *Adv. Mater.*, 2023, **35**(43), 2206625, DOI: 10.1002/adma.202206625.

5 J. Wang, B. Ge, H. Li, M. Yang, J. Wang, D. Liu, C. Fernandez, X. Chen and Q. Peng, Challenges and Progresses of Lithium-Metal Batteries, *Chem. Eng. J.*, 2021, **420**, 129739, DOI: 10.1016/j.cej.2021.129739.

6 N. S. Grundish, J. B. Goodenough and H. Khani, Designing Composite Polymer Electrolytes for All-Solid-State Lithium Batteries, *Curr. Opin. Electrochem.*, 2021, **30**, 100828, DOI: 10.1016/j.coelec.2021.100828.

7 P. Yao, H. Yu, Z. Ding, Y. Liu, J. Lu, M. Lavorgna, J. Wu and X. Liu, Review on Polymer-Based Composite Electrolytes for

Lithium Batteries, *Front. Chem.*, 2019, **7**, 522, DOI: 10.3389/fchem.2019.00522.

8 X. Yu and A. Manthiram, A Review of Composite Polymer-Ceramic Electrolytes for Lithium Batteries, *Energy Storage Mater.*, 2021, **34**, 282–300, DOI: 10.1016/j.ensm.2020.10.006.

9 S. C. Sand, J. L. M. Rupp and B. Yildiz, A Critical Review on Li-Ion Transport, chemistry and structure of ceramic-polymer composite electrolytes for solid state batteries, *Chem. Soc. Rev.*, 2025, DOI: 10.1039/D4CS00214H.

10 P. Fan, H. Liu, V. Marosz, N. T. Samuels, S. L. Suib, L. Sun and L. Liao, High Performance Composite Polymer Electrolytes for Lithium-Ion Batteries, *Adv. Funct. Mater.*, 2021, **31**(23), 2101380, DOI: 10.1002/adfm.202101380.

11 K. Xu, Electrolytes and Interphases in Li-Ion Batteries and Beyond, *Chem. Rev.*, 2014, **114**(23), 11503–11618, DOI: 10.1021/cr500003w.

12 D. K. Pradhan, B. K. Samantaray, R. N. P. Choudhary and A. K. Thakur, Effect of Plasticizer on Structure—Property Relationship in Composite Polymer Electrolytes, *J. Power Sources*, 2005, **139**(1), 384–393, DOI: 10.1016/j.jpowsour.2004.05.050.

13 L.-Z. Fan, X.-L. Wang, F. Long and X. Wang, Enhanced Ionic Conductivities in Composite Polymer Electrolytes by Using Succinonitrile as a Plasticizer, *Solid State Ion.*, 2008, **179**(27), 1772–1775, DOI: 10.1016/j.ssi.2008.01.035.

14 J. Seol, R. Balasubramaniam, V. Aravindan, R. Thangavel and Y.-S. Lee, Ameliorating the Electrode/Electrolyte Interface Compatibility in Li-Ion Solid-State Batteries with Plasticizer, *J. Alloys Compd.*, 2022, **927**, 167077, DOI: 10.1016/j.jallcom.2022.167077.

15 M. S. Michael, M. M. E. Jacob, S. R. S. Prabaharan and S. Radhakrishna, Enhanced Lithium Ion Transport in PEO-Based Solid Polymer Electrolytes Employing a Novel Class of Plasticizers, *Solid State Ionics*, 1997, **98**(3), 167–174, DOI: 10.1016/S0167-2738(97)00117-3.

16 H. T. Ahmed, V. J. Jalal, D. A. Tahir, A. H. Mohamad and O. G. Abdullah, Effect of PEG as a Plasticizer on the Electrical and Optical Properties of Polymer Blend Electrolyte MC-CH-LiBF4 Based Films, *Results Phys.*, 2019, **15**, 102735, DOI: 10.1016/j.rinp.2019.102735.

17 Y. Li, J. Wang, J. Tang, Y. Liu and Y. He, Conductive Performances of Solid Polymer Electrolyte Films Based on PVB/LiClO4 Plasticized by PEG200, PEG400 and PEG600, *J. Power Sources*, 2009, **187**(2), 305–311, DOI: 10.1016/j.jpowsour.2008.11.126.

18 S. Ibrahim, S. M. M. Yasin, R. Ahmad and M. R. Johan, Effects of Various EC Plasticizer Concentrations on Salted PEO Based Solid Polymer Electrolytes, *Int. J. Plast. Technol.*, 2012, **16**(2), 125–135, DOI: 10.1007/s12588-012-9034-4.

19 X. Qian, N. Gu, Z. Cheng, X. Yang, E. Wang and S. Dong, Plasticizer Effect on the Ionic Conductivity of PEO-Based Polymer Electrolyte, *Mater. Chem. Phys.*, 2002, **74**(1), 98–103, DOI: 10.1016/S0254-0584(01)00408-4.

20 H. M. J. C. Pitawala, M. A. K. L. Dissanayake, V. A. Seneviratne, B.-E. Mellander and I. Albinson, Effect of Plasticizers (EC or PC) on the Ionic Conductivity and Thermal Properties of the (PEO)9LiTf: Al_2O_3 Nanocomposite Polymer Electrolyte System, *J. Solid State Electrochem.*, 2008, **12**(7), 783–789, DOI: 10.1007/s10008-008-0505-7.

21 N. Meng, X. Zhu and F. Lian, Particles in Composite Polymer Electrolyte for Solid-State Lithium Batteries: A Review, *Particuology*, 2022, **60**, 14–36, DOI: 10.1016/j.partic.2021.04.002.

22 X. Lu, Y. Wang, X. Xu, B. Yan, T. Wu and L. Lu, Polymer-Based Solid-State Electrolytes for High-Energy-Density Lithium-Ion Batteries – Review, *Adv. Energy Mater.*, 2023, **13**(38), 2301746, DOI: 10.1002/aenm.202301746.

23 P. Yao, H. Yu, Z. Ding, Y. Liu, J. Lu, M. Lavorgna, J. Wu and X. Liu, Review on Polymer-Based Composite Electrolytes for Lithium Batteries, *Front. Chem.*, 2019, **7**, 522, DOI: 10.3389/fchem.2019.00522.

24 X. Yang, J. Liu, N. Pei, Z. Chen, R. Li, L. Fu, P. Zhang and J. Zhao, The Critical Role of Fillers in Composite Polymer Electrolytes for Lithium Battery, *Nano-Micro Lett.*, 2023, **15**(1), 74, DOI: 10.1007/s40820-023-01051-3.

25 M. A. K. L. Dissanayake, P. A. R. D. Jayathilaka, R. S. P. Bokalawala, I. Albinsson and B.-E. Mellander, Effect of Concentration and Grain Size of Alumina Filler on the Ionic Conductivity Enhancement of the (PEO)9LiCF3SO3: Al_2O_3 Composite Polymer Electrolyte, *J. Power Sources*, 2003, **119–121**, 409–414, DOI: 10.1016/S0378-7753(03)00262-3.

26 D. Yu, Z. C. Tronstad and B. D. McCloskey, Lithium-Ion Transport and Exchange between Phases in a Concentrated Liquid Electrolyte Containing Lithium-Ion-Conducting Inorganic Particles, *ACS Energy Lett.*, 2024, **9**(4), 1717–1724, DOI: 10.1021/acsenergylett.4c00502.

27 L. Porcarelli, P. Sutton, V. Bocharova, R. H. Aguirresarobe, H. Zhu, N. Goujon, J. R. Leiza, A. Sokolov, M. Forsyth and D. Mecerreyes, Single-Ion Conducting Polymer Nanoparticles as Functional Fillers for Solid Electrolytes in Lithium Metal Batteries, *ACS Appl. Mater. Interfaces*, 2021, **13**(45), 54354–54362, DOI: 10.1021/acsami.1c15771.

28 P. Raghavan, X. Zhao, J.-K. Kim, J. Manuel, G. S. Chauhan, J.-H. Ahn and C. Nah, Ionic Conductivity and Electrochemical Properties of Nanocomposite Polymer Electrolytes Based on Electrospun Poly(Vinylidene Fluoride-Co-Hexafluoropropylene) with Nano-Sized Ceramic Fillers, *Electrochim. Acta*, 2008, **54**(2), 228–234, DOI: 10.1016/j.electacta.2008.08.007.

29 Z. Ali, S. Yaqoob, J. Yu and A. D'Amore, Critical Review on the Characterization, Preparation, and Enhanced Mechanical, Thermal, and Electrical Properties of Carbon Nanotubes and Their Hybrid Filler Polymer Composites for Various Applications, *Composites, Part C*, 2024, **13**, 100434, DOI: 10.1016/j.jcomc.2024.100434.

30 S. Park, Y.-W. Song, B. Ryu, H. Son, M.-Y. Kim, J. Kim, J. Lim and C. Yun, 3D Current Collector Based on Cellulose-Carbon Nanotube Nanocomposites for All-Solid-State Batteries, *J. Mater. Chem. A*, 2024, **12**(37), 25530–25544, DOI: 10.1039/D4TA04378B.

31 T. Fuchs, C. G. Haslam, A. C. Moy, C. Lerch, T. Krauskopf, J. Sakamoto, F. H. Richter and J. Janek, Increasing the Pressure-Free Stripping Capacity of the Lithium Metal Anode in Solid-State-Batteries by Carbon Nanotubes, *Adv. Energy Mater.*, 2022, **12**(26), 2201125, DOI: 10.1002/aenm.202201125.

32 Z. Deng, S. Chen, K. Yang, Y. Song, S. Xue, X. Yao, L. Yang and F. Pan, Tailoring Interfacial Structures to Regulate Carrier Transport in Solid-State Batteries, *Adv. Mater.*, 2024, **36**(38), 2407923, DOI: 10.1002/adma.202407923.

33 M. J. Counihan, D. J. Powers, P. Barai, S. Hu, T. Zagorac, Y. Zhou, J. Lee, J. G. Connell, K. S. Chavan, I. S. Gilmore, L. Hanley, V. Srinivasan, Y. Zhang and S. Tepavcevic, Understanding the Influence of Li7La3Zr2O12 Nanofibers on Critical Current Density and Coulombic Efficiency in Composite Polymer Electrolytes, *ACS Appl. Mater. Interfaces*, 2023, **15**(21), 26047–26059, DOI: 10.1021/acsami.3c04262.

34 P. Barai, T. Fuchs, E. Trevisanello, H. K. Kim, F. H. Richter, J. Janek and V. Srinivasan, Reaction Current Heterogeneity at the Interface between a Lithium Electrode and Polymer/Ceramic Composite Electrolytes, *ACS Appl. Energy Mater.*, 2023, **6**(4), 2160–2177, DOI: 10.1021/acsaem.2c03059.

35 M. A. K. L. Dissanayake, P. A. R. D. Jayathilaka, R. S. P. Bokalawala, I. Albinsson and B.-E. Mellander, Effect of Concentration and Grain Size of Alumina Filler on the Ionic Conductivity Enhancement of the (PEO)9LiCF3SO3: Al_2O_3 Composite Polymer Electrolyte, *J. Power Sources*, 2003, **119–121**, 409–414, DOI: 10.1016/S0378-7753(03)00262-3.

36 S. Klongkan and J. Pumchusak, Effects of Nano Alumina and Plasticizers on Morphology, Ionic Conductivity, Thermal and Mechanical Properties of PEO-LiCF3SO3 Solid Polymer Electrolyte, *Electrochim. Acta*, 2015, **161**, 171–176, DOI: 10.1016/j.electacta.2015.02.074.

37 Y.-C. Huang, Y.-L. Chu, C.-C. Chang, L.-Y. Liu, H. Teng, B.-H. Chen and J.-S. Jan, Ultraviolet-Cured Composite Polymer Electrolyte Containing Deep-Eutectic-Solvent and Aluminum Oxide Filler for Lithium-Metal Batteries with Enhanced Cycle Life, *J. Electroanal. Chem.*, 2023, **940**, 117455, DOI: 10.1016/j.jelechem.2023.117455.

38 E. M. Masoud, A.-A. El-Bellihi, W. A. Bayoumy and M. A. Mousa, Organic–Inorganic Composite Polymer Electrolyte Based on PEO–LiClO4 and Nano-Al_2O_3 Filler for Lithium Polymer Batteries: Dielectric and Transport Properties, *J. Alloys Compd.*, 2013, **575**, 223–228, DOI: 10.1016/j.jallcom.2013.04.054.

39 F. Croce, G. B. Appetecchi, L. Persi and B. Scrosati, Nanocomposite Polymer Electrolytes for Lithium Batteries, *Nature*, 1998, **394**(6692), 456–458, DOI: 10.1038/28818.

40 M. Rumpel, L. Appold, J. Baber, W. Stracke, A. Flegler and G. Sextl, Impact of the Sintering Additive Li 3 PO 4 on the Sintering Behaviour, Microstructure and Electrical Properties of a Ceramic LATP Electrolyte, 2022. DOI: 10.1039/D2MA00655C.

41 R. Gurusamy, A. Lakshmanan, N. Srinivasan and S. Venkatachalam, Incorporating LLTO Ceramic into PVDF/PEO Polymer Electrolyte for Lithium-Ion Capacitor, *J. Electroanal. Chem.*, 2024, **957**, 118135, DOI: 10.1016/j.jelechem.2024.118135.

42 D. Brogioli, F. Langer, R. Kun and F. La Mantia, Space-Charge, Effects at the Li7La3Zr2O12/Poly(Ethylene Oxide) Interface, *ACS Appl. Mater. Interfaces*, 2019, **11**(12), 11999–12007, DOI: 10.1021/acsami.8b19237.

43 P. Ranque, J. Zagórski, S. Devaraj, F. Aguesse and J. M. L. del Amo, Characterization of the Interfacial Li-Ion Exchange Process in a Ceramic–Polymer Composite by Solid State NMR, *J. Mater. Chem. A*, 2021, **9**(33), 17812–17820, DOI: 10.1039/D1TA03720J.

44 T. Yang, J. Zheng, Q. Cheng, Y.-Y. Hu and C. K. Chan, Composite Polymer Electrolytes with Li7La3Zr2O12 Garnet-Type Nanowires as Ceramic Fillers: Mechanism of Conductivity Enhancement and Role of Doping and Morphology, *ACS Appl. Mater. Interfaces*, 2017, **9**(26), 21773–21780, DOI: 10.1021/acsami.7b03806.

45 M. J. Counihan, J. Lee, P. Mirmira, P. Barai, M. E. Burns, C. V. Amanchukwu, V. Srinivasan, Y. Zhang and S. Tepavcevic, Improved Interfacial Li-Ion Transport in Composite Polymer Electrolytes via Surface Modification of LLZO, *Energy Mater.*, 2025, **5**, 500032, DOI: 10.20517/energymater.2024.195.

46 M. M. U. Din, M. Häusler, S. M. Fischer, K. Ratzenböck, F. F. Chamasemani, I. Hanghofer, V. Henninge, R. Brunner, C. Slugovc and D. Rettenwander, Role of Filler Content and Morphology in LLZO/PEO Membranes, *Front. Energy Res.*, 2021, **9**, 711610, DOI: 10.3389/fenrg.2021.711610.

47 M. R. Bonilla, F. A. García Daza, P. Ranque, F. Aguesse, J. Carrasco and E. Akhmatskaya, Unveiling Interfacial Li-Ion Dynamics in Li7La3Zr2O12/PEO(LiTFSI) Composite Polymer-Ceramic Solid Electrolytes for All-Solid-State Lithium Batteries, *ACS Appl. Mater. Interfaces*, 2021, **13**(26), 30653–30667, DOI: 10.1021/acsami.1c07029.

48 A. Kondori, M. Esmaeilirad, A. M. Harzandi, R. Amine, M. T. Saray, L. Yu, T. Liu, J. Wen, N. Shan, H.-H. Wang, A. T. Ngo, P. C. Redfern, C. S. Johnson, K. Amine, R. Shahbazian-Yassar, L. A. Curtiss and M. Asadi, A Room Temperature Rechargeable Li2O-Based Lithium-Air Battery Enabled by a Solid Electrolyte, *Science*, 2023, **379**(6631), 499–505, DOI: 10.1126/science.abq1347.

49 C. Yan, P. Zhu, H. Jia, Z. Du, J. Zhu, R. Orenstein, H. Cheng, N. Wu, M. Dirican and X. Zhang, Garnet-Rich Composite Solid Electrolytes for Dendrite-Free, High-Rate, Solid-State Lithium-Metal Batteries, *Energy Storage Mater.*, 2020, **26**, 448–456, DOI: 10.1016/j.ensm.2019.11.018.

50 E. Kuhnert, L. Ladenstein, A. Jodlbauer, C. Slugovc, G. Trimmel, H. M. R. Wilkening and D. Rettenwander, Lowering the Interfacial Resistance in Li6.4La3Zr1.4Ta0.6O12|Poly(Ethylene Oxide) Composite Electrolytes, *Cell Rep. Phys. Sci.*, 2020, **1**(10), 100214, DOI: 10.1016/j.xcrp.2020.100214.

51 L. Helmers, F. Frankenberg, J. Brokmann, C. Burmeister, A. Buchheit, A. Kwade and P. Michalowski, Functionalized

Thiophosphate and Oxidic Filler Particles for Hybrid Solid Electrolytes, *ChemElectroChem*, 2023, **10**(21), e202300310, DOI: 10.1002/celc.202300310.

52 F. H. Haghighi, M. Mercurio, S. Cerra, T. A. Salamone, R. Bianymotlagh, C. Palocci, V. R. Spica and I. Fratoddi, Surface Modification of TiO2 Nanoparticles with Organic Molecules and Their Biological Applications, *J. Mater. Chem. B*, 2023, **11**(11), 2334–2366, DOI: 10.1039/D2TB02576K.

53 A. Vaitkus, A. Merkys and S. Gražulis, Validation of the Crystallography Open Database using the Crystallographic Information Framework, *J. Appl. Crystallogr.*, 2021, **54**, 661–672.

54 A. Vaitkus, *et al.*, A workflow for deriving chemical entities from crystallographic data and its application to the Crystallography Open Database, *J. Cheminform.*, 2023, **15**, 123.

55 A. Merkys, *et al.*, Graph isomorphism-based algorithm for cross-checking chemical and crystallographic descriptions, *J. Cheminform.*, 2023, **15**, 25.

56 K. Momma and F. Izumi, *VESTA* 3 for three-dimensional visualization of crystal, volumetric and morphology data, *J. Appl. Crystallogr.*, 2011, **44**, 1272–1276.

57 G. Kresse and J. Furthmüller, Efficient iterative schemes for *ab initio* total-energy calculations using a plane-wave basis set, *Phys. Rev. B:Condens. Matter Mater. Phys.*, 1996, **54**, 11169–11186.

58 G. Kresse and J. Furthmüller, Efficiency of *ab initio* total energy calculations for metals and semiconductors using a plane-wave basis set, *Comput. Mater. Sci.*, 1996, **6**, 15–50.

59 G. Kresse and J. Hafner, *Ab initio* molecular dynamics for liquid metals, *Phys. Rev. B:Condens. Matter Mater. Phys.*, 1993, **47**, 558–561.

60 G. Kresse and D. Joubert, From ultrasoft pseudopotentials to the projector augmented-wave method, *Phys. Rev. B: Condens. Matter Mater. Phys.*, 1999, **59**, 1758–1775.

61 J. P. Perdew, K. Burke and M. Ernzerhof, Generalized Gradient Approximation Made Simple, *Phys. Rev. Lett.*, 1996, **77**, 3865–3868.

62 A. Kondori, *et al.*, A room temperature rechargeable Li_2O-based lithium-air battery enabled by a solid electrolyte, *Science*, 2023, **379**, 499–505.

63 E. Barsoukov and J. R. Macdonald, *Impedance Spectroscopy: Theory, Experiment, and Applications*, Wiley, Hoboken, NJ, 2nd edn, 2005.

64 G. J. Simon, M. Hanauer, F. Richter and J. Janek, Interphase Formation of PEO_{20}:LiTFSI–Li_6PS_5Cl Composite Electrolytes with Lithium Metal, *ACS Appl. Mater. Interfaces*, 2020, **12**(10), 11773–11782, DOI: 10.1021/acsami.9b22968.

65 B. X. Dong, P. Bennington, Y. Kambe, D. Sharon, M. Dolejsi, J. Strzalka, V. F. Burnett, P. F. Nealey and S. N. Patel, *Mol. Syst. Des. Eng.*, 2019, **4**, 597–608.